Current Applied Materials, 2022, *1*, e110122200128

RESEARCH ARTICLE

Evaluation of Rare-earth Sesquioxides Nanoparticles as a Bottom-up Strategy Toward the Formation of Functional Structures

Silas Cardoso dos Santos[1,*], Orlando Rodrigues Junior[1] and Leticia Lucente Campos[1]

[1]*Radiation Dosimetry Center, Instituto de Pesquisas Energéticas e Nucleares, Avenida Lineu Prestes 2242, Cidade Universitária, Sao Paulo, Brazil*

ARTICLE HISTORY

Received: July 26, 2021
Revised: October 05, 2021
Accepted: October 15, 2021

DOI: *10.2174/2666731201666220111102037*

Abstract: ***Background*:** The strategy to form functional structures based on powder technology relies on the concept of nanoparticles characteristics. Rare-earth sesquioxides (RE_2O_3; RE as Y, Tm, Eu) exhibit remarkable properties, and their fields of application include energy, astronomy, environmental, medical, information technology, industry, and materials science. The purpose of this paper is to evaluate the characteristics of RE_2O_3 nanoparticles as a bottom-up strategy to form functional materials for radiation dosimetry.

***Methods*:** The RE_2O_3 nanoparticles were characterized by the following techniques: XRD, SEM, PCS, FTIR, ICP, EPR, and zeta potential.

***Results*:** All RE_2O_3 samples exhibited cubic C-type structure in accordance with the sesquioxide diagram, chemical composition over 99.9 %, monomodal mean particle size distribution, in which d_{50} value was inferior to 130 nm. Among all samples, only yttrium oxide exhibited an EPR signal, in which the most intense peak was recorded at 358mT and g 1.9701.

***Conclusion*:** Evaluating nanoparticle characteristics is extremely important by considering a bottom-up strategy to form functional materials. The RE_2O_3 nanoparticles exhibit promising characteristics for application in radiation dosimetry.

Keywords: Rare-earths, sesquioxides, nanoparticles, functional structures, radiation dosimetry, ceramic processing

1. INTRODUCTION

The strategy to form functional structures based on powder technology relies on the concept of nanoparticles characteristics. In general, nanoparticles are ultrafine particles that are nanometer in size ranging from 1 to 1000nm [1]. Particles at a nanometer scale tend to be affected by their own atoms and molecules, exhibiting different properties from their bulk constituting the same solid substance/material [2-5]. Besides, nanoparticle characteristics, such as size [6], shape [7], density [8], and chemical composition [9], directly affect the material/end-use component characteristics. Therefore, the characterization of nanoparticles is a very important step toward the formation of new functional structures.

Rare-earth sesquioxides (RE_2O_3; RE as a metal atom) exhibit remarkable proprieties, and their fields of investigation and application include energy [10], economy [11], environmental [12], medical [13], information technology [14], industry [15], and materials science [16]. Considering the vast applicability of the rare-earth materials and China's domination in rare-earth production [17], The United States of America [18] and the European Union [19] classified rare-earths as critical materials.

The use of a small quantity of rare-earth in the formulation of new structures has led to the development of new materials with improved characteristics [20-24]. Zhao *et al*. [25] reported that using Tb^{3+} and Yb^{3+} as activators of silicate glasses improved the efficiency of the solar cell down-conversion layer by up 8.6 %. Djamal *et al*. [26] observed that the amount of 1.0 mol. % Dy_2O_3 improved the glass medium structure and provided light emission in the visible region induced by x-ray. Kershi *et al*. [27] revealed that low concentrations of Er^{3+} ($\gamma \leq 0.14$) improved the elastic moduli of $Er_\gamma Zn_{0.2}Co_{0.8}Fe_{2-\gamma}O_4$ (E-ZCFNs) compounds.

Based on the information mentioned above, the purpose of this paper is to evaluate the characteristics of RE_2O_3 sesquioxides (RE_2O_3; RE as Y, Tm, Eu) as a bottom-up strategy to form functional materials for radiation dosimetry.

2. MATERIALS AND METHODS

The term sesquioxide (RE_2O_3, RE means the rare-earth metal) was assigned to the following rare-earth oxides: yttria (Y_2O_3, 99.99 %, Alfa Aesar GmbH), thulium oxide (Tm_2O_3, 99.999 %, Alfa Aesar GmbH), and europium oxide (Eu_2O_3, 99.999 %, Alfa Aesar GmbH).

*Address correspondence to this author at the Radiation Dosimetry Center, Instituto de Pesquisas Energéticas e Nucleares, Avenida Lineu Prestes 2242, Cidade Universitária, Sao Paulo, Brazil;
E-mail: silas.cardoso@alumni.usp.br

2666-7339/22 $65.00+.00

The RE_2O_3 particles as received were characterised using the following techniques: Fourier Transform Infrared Spectroscopy (FTIR, Thermo Nicolet iS50), Inductively Coupled Plasma Atomic Emission Spectroscopy (ICP/AES, ICPE 9000, Shimadzu), Scanning Electron Microscopy with respect to particle size and shape (SEM, INCAx-act, Oxford Instruments), and Photon Correlation Spectroscopy with respect to particle size distribution (d_{10}, d_{50}, d_{90}) (PCS, Litesizer500, Anton Paar), where the mean diameter size (d_{50}) was calculated based on hydrodynamic diameter model Eq. (**1**) [28].

$$d_{50} = \left(\frac{K_{BT}}{3\pi\eta(T)D_t}\right)[nm] \quad (1)$$

Where, K_{BT} is the Boltzmann constant, T is the temperature (K), h (T) is the viscosity of the liquid, and D_t is the particle diffusion coefficient.

The crystalline structures of the RE_2O_3 powders were evaluated by X-ray diffraction (XRD, Rigaku Multiflex, Japan), with an angular range of (2θ) 15-70º, scanning of 0.5º.min^{-1}, and Kα source. The crystallite sizes (d_c) were calculated by the Scherrer model [41] (Eq. (**2**)), based on the measurement of full-width at half-maximum (FWHM) [29] values. The crystalline structures of samples were identified according to the Powder Diffraction File (PDF).

$$d_c = \left(\frac{k.\lambda}{\beta cos\theta}\right)[nm] \quad (2)$$

Where, k is 0.9 for spherical shape factor; λ is 1.54 Å for the wavelength of the CuKα radiation, θ is the angle of diffraction, and β is FWHM of the peak.

The true density (ρ) was measured by using a helium pycnometer (Micrometrics 1330), where ρ is expressed according to Eq. (**3**).

$$\rho = \left(\frac{N_a V_m A_m}{V_{mol} M_s}\right)[m^2.g^{-1}] \quad (3)$$

Where, N_A is the Avogadro constant (6.023.10^{23} mol^{-1}), A_M is the adsorbed gas area (16.2.10^{-20}m^2 for N_2 and 19.5.10^{-20} m^2 for Kr), V_M is the adsorbed gas molecule volume, V_{mol} corresponds to 1mol gas volume under environmental temperature, and Ms is the sample mass.

The paramagnetic response of RE_2O_3 nanoparticles was evaluated by electron paramagnetic resonance using an X-band EPR spectrometer (Bruker EMX PLUS). All EPR spectra were recorded under the following conditions: environmental atmosphere, field modulation frequency of 100 kHz, microwave power of 2.5 mW, center field of 300 mT, sweep width of 300 mT, modulation amplitude of 0.4 mT, time constant of 0.01 ms, 10 scans, temperature at 20 ºC, and controlled humidity using DPPH (2, 2-Diphenyl-1-picrylhydrazyl, Bruker) as reference. The g values were calculated based on Eq. (**4**).

$$g = 714.4775.\left(\frac{v_{[GHz]}}{\beta_{0\,[G]}}\right)[a.u.] \quad (4)$$

Where, v is microwave frequency in (GHz), and β_0 is a magnetic field in (G).

Zeta potential (z) evaluation of RE_2O_3 in an aqueous medium was performed by a light scattering analyzer (Litesizer 500, Anto Paar), constituted of a laser beam of wavelength 658nm, power 40mW, and detection angle of 15º. In addition, z values were calculated according to Eq. (**5**). Aqueous suspensions were prepared with 0.5 g·L^{-1} solids and NaCl 10^{-3} M (58.44 g.mol^{-1}, Merck). HCl and KOH solutions were used to adjust the pH of the suspensions from acid to alkaline conditions (pH 5.6 – 11).

$$\zeta = \frac{6\pi\eta\mu_e}{\varepsilon f(k\alpha)}[mV] \quad (5)$$

Where,

- ε = electric permissively;
- η = viscosity of medium [mPa.s];
- μ_e = electrophoretic mobility [μ.s^{-1}.V^{-1}.cm];
- f(kα) = 1.5 (aqueous solvent).

3. RESULTS AND DISCUSSION

The X-ray curves of RE_2O_3 nanoparticles are illustrated in Fig. (**1a**). The Y_2O_3 sample exhibited diffraction peak characteristics of the body-centered cubic structure- bcc (PDF.71-99), with high intense diffraction peak recorded at 29º plane (211), space group I_{a-3}, 16 unity cells, and 32 cations [30]. Among 32 cations, 8 were located at $C_{3i,6}$ and 24 were located at C_2. The C_{3i},S_6 exhibited an inversion center and smaller crystal fields, which did not provide electron-dipole transitions. On the other hand, the C_2 axis did not exhibit an inversion center, making electron-dipole transitions possible. Filling the C_2 axis with RE ions intensified the luminescence response of Y_2O_3, as reported in previous studies [31-35].

The Tm_2O_3 nanoparticles exhibited cubic C-type structure Fig. (**1a**), space group I_{a-3}, with a high peak intensity recorded at 29º, plane (211), fitting to (PDF 78-389). Moreover, it has been observed that Eu_2O_3 nanoparticles Fig. (**1**) exhibited sharp diffraction peaks, like yttria and thulium oxide, but no second phase was identified. Possibly, a prior thermal treatment should improve the crystalline aspect of the powders. The most intense peak was recorded at 28º according to the plane (222) and PDF (65-3182).

In general, rare-earth sesquioxides exhibit similar diffraction patterns due to their physical properties, and the crystal identification is achieved in the order of slight difference between the diffraction planes. Fig. (**1b**) illustrates the polymorphic diagram of the sesquioxides as a function of temperature, where all the possible structures (A, B, C, X, and H) are represented. According to the diagram, the type C structure presents the widest phase field, covering all RE groups (from La to Lu). For europium oxide, the cubic C-type structure remains stable up to 1000 ºC, whereas for thulium oxide, the stability is maintained up to 2200 ºC.

Controversial data have been reported in the literature regarding the crystalline structure of yttrium oxide powders. Qin *et al*. [36] observed that nanoparticles with diameter sizes smaller than 10nm exhibited polymorphism from cubic c-type to monoclinic. Gourlaouen *et al*. [37] synthesized nanoparticles with a monoclinic structure by hot pressing under 997 C and 2 GPa. Navrostky *et al*. [38] reported that yttrium oxide samples presented the following structural changes: cubic c-type → fluorite → hexagonal. During our

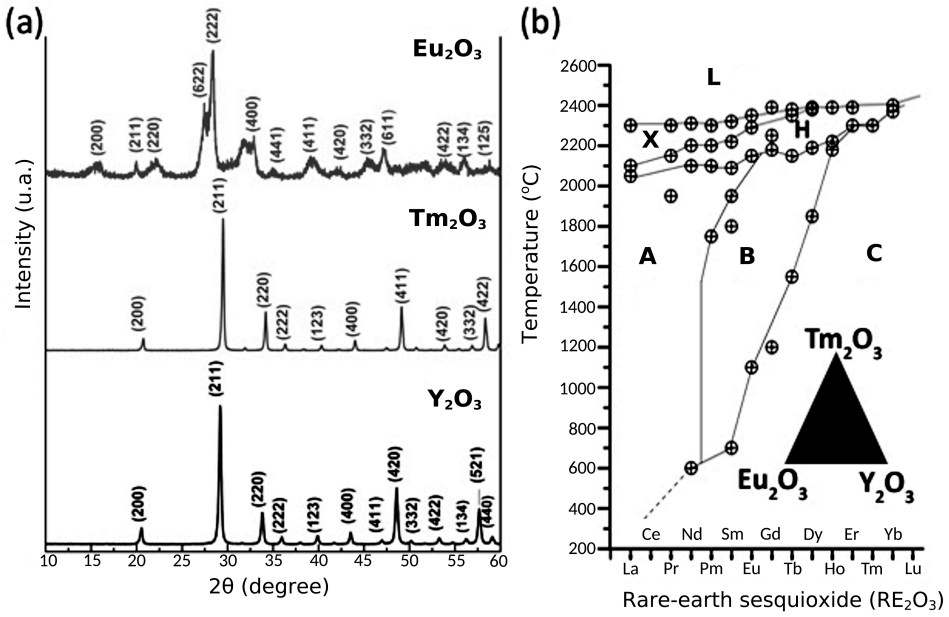

Fig. (1). X-ray curves of R_2O_3 powders: (**a**) Y_2O_3, Tm_2O_3, and Eu_2O_3; (**b**) crystal structure formation diagram (A, B, C, X, L, and H) of the rare-earth sesquioxides as a function of temperature. (*A higher resolution / colour version of this figure is available in the electronic copy of the article*).

investigation on yttrium-dysprosium ceramics [39], it was observed that ceramic samples exhibited cubic C-type structure, even though a significant quantity of dysprosium was used (19 wt.%). This result is in agreement with the illustration of the polymorph diagram, and the cubic C-type form is found to be the most favourable structure to be formed for most rare-earth sesquioxides.

The mean particle size distribution curves of RE_2O_3 powders are illustrated in Fig. (**2**). Samples of Y_2O_3 Fig. (**2a**), Eu_2O_3 Fig. (**2b**) and Tm_2O_3 Fig. (**2c**) exhibited a particle size distribution in nano-sized range, with the following parameters: mean diameter (d_{50}) as 112nm, 89nm, and 162nm, dispersion less than 3nm ($d_{90} - d_{10}$), and relative dispersion (dispersion/d_{50}) less than 0.03. Dispersion values close to zero (0) are an indication that the particle size distribution curves exhibit data very close to the unitary particle size.

Particle size distribution in the nano-sized range is beneficial to provide ceramic bodies with dense microstructure and homogeneous grain size distribution. Nanoparticles exhibit high specific surface area ($m^2.g^{-1}$), which means more contact between particles after shaping. Besides, nanoparticles usually undergo sintering at a lower temperature than the coarse ones. Furthermore, several studies have reported that particle size is a key parameter to enhance materials characteristics [40-43]. Okuyama *et al*. [44] reported that the photoluminescence and quantum efficiency of yttrium oxide particles rely on particle and crystallite sizes, where the powders are composed of particles with a diameter size of 500nm and crystallite size around 40 nm exhibited the best photoluminescence results.

SEM images of the RE_2O_3 powders as received, *i.e*., with no previous processing, are illustrated in Fig. (**3**). According to the results, the three sesquioxides are constituted by agglomerates of flake particles. The formation of these agglomerates can be due to previous processing stages (synthesis, mixing, thermal treatment) and the preparation approach of samples for SEM. Even though particles exhibit a mean particle size distribution in the nano-sized range, as shown in Fig. (**2**), they tend to form large agglomerates due to attraction forces (electrostatic, structural, and Van der Waals).

The samples of Tm_2O_3 Fig. (**3a**) and Y_2O_3 Fig. (**3c**) exhibited broad flakes, and their sizes were larger than 1μm, whereas Eu_2O_3 powders Fig. (**3b**) whose particle size was smaller than 500 nm, presented very narrow flakes. It is known that powder synthesis and processing influence the characteristics of particles [45-48]. Relevant studies have reported that particle shape and size can be controlled by synthesis methods, where particles with spherical [49], hollow [50], elongated [51], flower-like [52], platelet-like [53], and acicular [54] shapes were obtained.

Additionally, the microstructure evolution of a powder compact relies on powder characteristics. Based on Dupont *et al*. [55] model, the sintering and densification of thin irregular platelet particles occur in four stages as follows: (1) shape transformation from irregular form to spherical shape (spheroid), (2) motion of particles, (3) densification, (4) grain growth Fig. (**3d**). Considering the characteristics of the rare-earth sesquioxides powders, these samples will probably undergo this sintering model as thermally treated.

Chemical-composition analysis results of RE_2O_3 powders by ICP are presented in Table **1**. Y_2O_3 powders were constituted by the majority of Y (550 ppm), followed by Cs (65 ppm), and a fraction of other constituents around 10 ppm. Eu_2O_3 powders exhibited the following main constituents: Eu (>1000 ppm), fractions of Cs (280 ppm), and Rh (22 ppm), including other minority elements with quantity inferior to 5 ppm. Tm_2O_3 powders were basically constituted by Tm (>1000 ppm), Cs (800 ppm), Rb (140 ppm), Rh (52 ppm), and

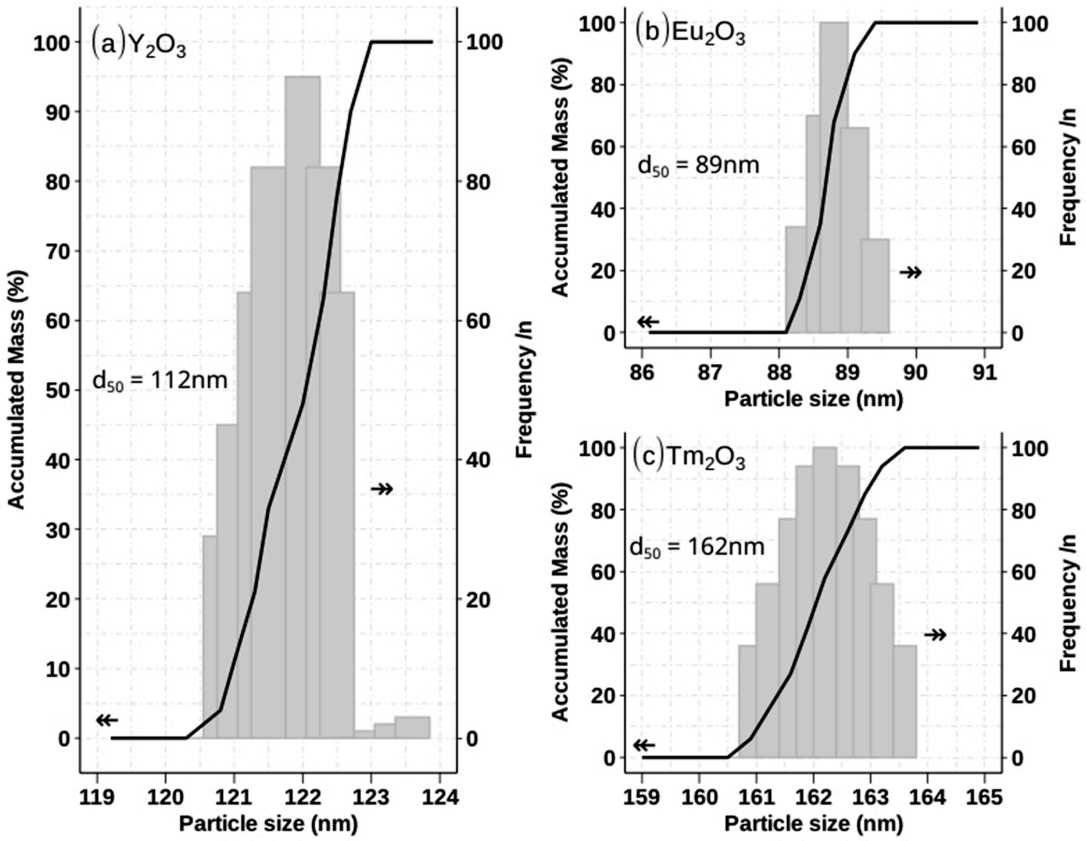

Fig. (2). Particle size distribution of RE_2O_3 powders by PCS: (**a**) Y_2O_3, (**b**) Eu_2O_3, and (**c**) Tm_2O_3. (*A higher resolution / colour version of this figure is available in the electronic copy of the article*).

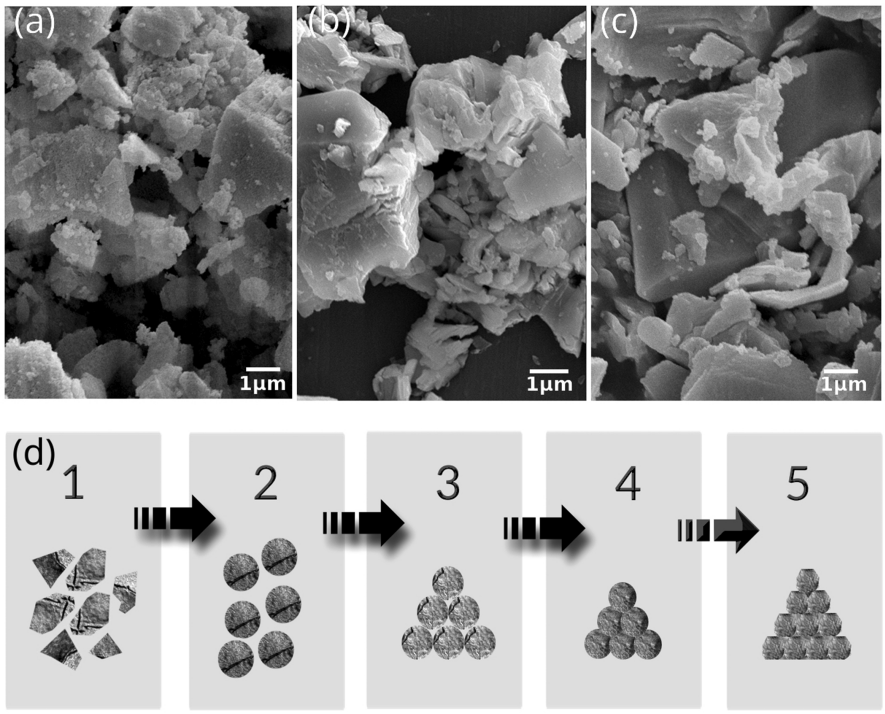

Fig. (3). Morphological characterization of RE_2O_3 powders by SEM: (**a**)Tm_2O_3, (**b**) Eu_2O_3, (**c**) Y_2O_3; and (**d**) sintering-densification particle model proposed by Dupont *et al*. [55]. (*A higher resolution / colour version of this figure is available in the electronic copy of the article*).

Table 1. Chemical composition of RE_2O_3 powders by ICP.

Substance	Element	Composition (ppm)	Element	Composition (ppm)
Y_2O_3	Y	550	Rh	3,5
	Cs	65	Ge	1,3
	Si	4,1	Pt	1,1
Eu_2O_3	Eu	>1000	U	2,2
	Cs	280	Cu	1,5
	Rh	22	P	1,5
	Si	4,4	Pr	1,4
	Th	3,9		
Tm_2O_3	Tm	>1000	Co	12
	Cs	800	Th	12
	Rb	140	Ir	5,9
	Rh	52	Si	4,3
	-	-	-	-

Table 2. Complementary characterization results of RE_2O_3 powders.

-	Y_2O_3	Eu_2O_3	Tm_2O_3
d_{50} (nm)	122.0	89.0	162.0
d_c (nm)	9.4	1.5	8.8
ρ_p (g.cm^{-3})	4.93	7.29	8.68
ρ_t (g.cm^{-3})	5.01	7.42	8.91

d_{50}: mean particle size by PCS; d_c: crystallite size; ρ_p: pycnometric density; ρ_t: theoretical density.

minority fractions below 15 ppm. The results revealed that all samples presented high purity levels, providing substantial parameters to advance toward the formation of new dosimetric materials.

The chemical composition of a substance is a key parameter to develop dosimetric materials. Undesired impurities can affect the further stages of colloidal processing, such as incomplete synthesis, formation of secondary phases, difficulties in preparing stable suspensions, microstructure defects, and low dosimetric response.

Complementary results regarding powder characterization of RE_2O_3 powders are shown in Table **2**. According to the results, all samples exhibited a mean particle diameter in a nano-sized range, crystalline size inferior to 10nm, and density values over 97 % of theoretical density.

The FT-IR spectra of RE_2O_3 powders are illustrated in Fig. (**4**). The Tm_2O_3 spectra revealed (1-3) peaks at 3504, 1510, and 1521 cm^{-1} related to M-OH bonds (M means Tm), whereas peak (4) was recorded at 620 cm^{-1} corresponded to M-O bonds [56]. It was observed for Y_2O_3 powders peaks recorded at 420, 463 e 566 cm^{-1} (1-3) related to Y-O radicals [57, 58]. The peaks recorded at 1395 and 1514 cm^{-1} represented C-O and C=O bonds due to CO_2 adsorption from the environment by KBr disks, as reported by Mangalajara *et al*. [59]. The peak (6) recorded at 3510 cm^{-1} was attributed to O-H radicals on the surface of yttrium-oxide particles [60]. The Eu_2O_3 spectra revealed peaks at 635, 754, and 880cm^{-1} (1-3) attributed to Eu-OH [61], peaks (4-7) recorded at 1375, 1494, and 1639 cm^{-1} due to asymmetric stretching of COO- bonds [62], and peaks (8-10) recorded at 3047, 3404, and 3602 cm^{-1} associated with adsorbed water on the particle surface [63].

The EPR spectra of Y_2O_3 recorded under environmental temperature and magnetic field range up to 600mT are illustrated in Fig. (**5**). Y_2O_3 powders presented three resonance peaks, and the most significant signal was recorded at 358 mT and g 1.9701 (p_1) associated with intrinsic defects, such as oxygen vacancies presented in cubic C-type. The lower intensity peaks recorded at 354 mT (g_2 1.9901-p_2) and 347 mT (g_3 2.0371-p_3) may be associated with material impurities, as well as new radicals formed during powder processing. Bordun *et al*. [64] reported that the luminescence response of Y_2O_3 was associated with its crystal characteristics (sites C_2 and S_6) and the chemical composition. According to the study conducted by Osipov *et al*. [65], Y_2O_3

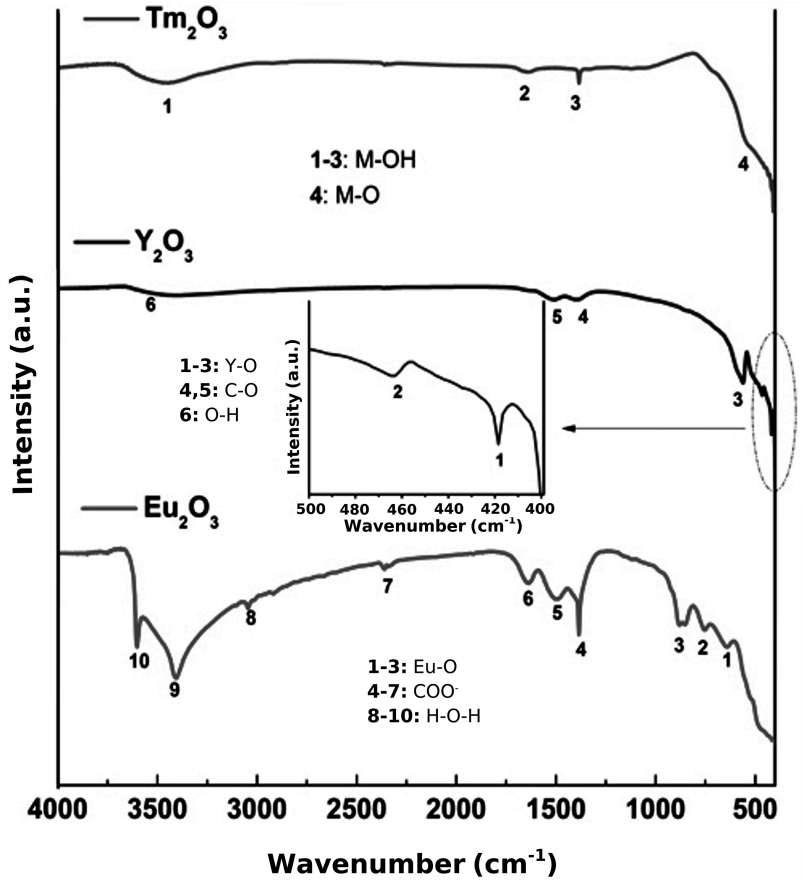

Fig. (4). FT-IR spectra of RE_2O_3 powders. (*A higher resolution / colour version of this figure is available in the electronic copy of the article*).

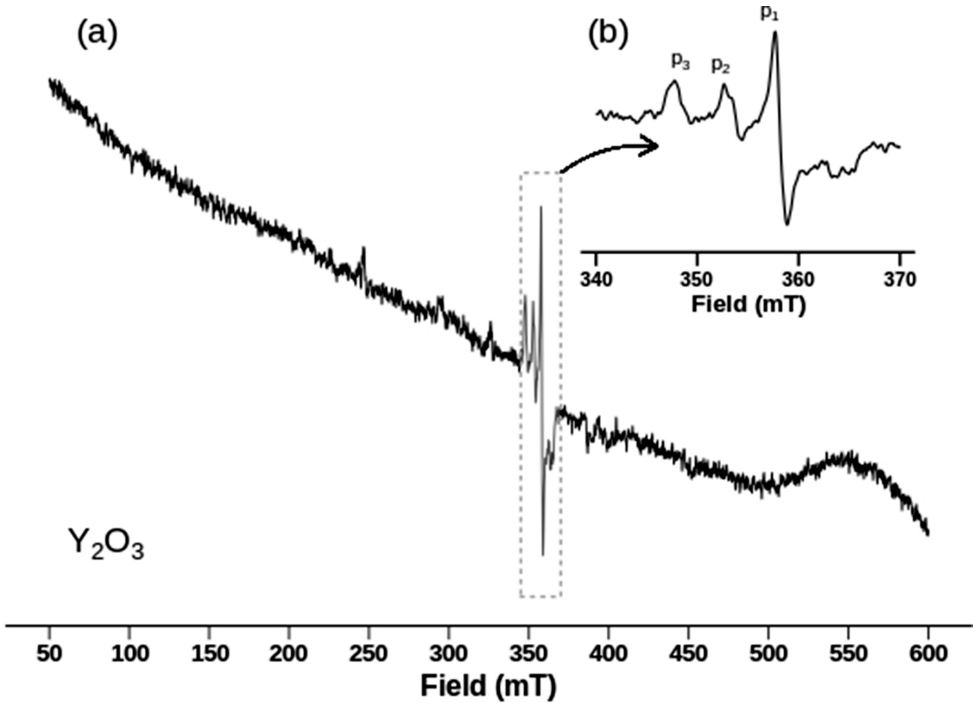

Fig. (5). EPR spectra of Y_2O_3 powders recorded under environmental temperature. (*A higher resolution / colour version of this figure is available in the electronic copy of the article*).

crystal structure presents YO radicals on crystal boundaries, which are responsible for improving the luminescence response.

Unfortunately, the following samples, Tm_2O_3 (Fig. **6a**) and Eu_2O_3 (Fig. **6b**), did not exhibit EPR response under environmental temperature. Possibly, the identification of their intrinsic radicals should be performed under low temperatures. Even though rare-earth sesquioxides usually exhibit many chemical and physical similarities, in this study, a divergence was observed. Therefore, additional investigations with a wider scope are necessary to identify these intrinsic defects precisely.

The zeta potential (ζ) characterization is a strategy to form advanced structures for radiation dosimetry. Zeta potential curves of RE oxides as a function of pH are illustrated in Fig. (**7a**). Below pH 8, only the samples of Eu_2O_3 and Tm_2O_3 exhibited significant zeta potential values, 37mV at pH 6.7 and 36mV at pH 6.1, respectively. On the other hand, above pH 10 (alkaline condition), substantial zeta values were observed for Y_2O_3 = 34mV at pH 10.9, Eu_2O_3 = 28 mV at pH 10.8, and Tm_2O_3 =24mV at pH 10.8.

The isoelectric point (IEP) means the pH value where zeta potential is 0; therefore, no dispersion mechanism occurs. The mean IEP values of RE samples were recorded as follows: Eu_2O_3 (9.1± 0.03), Tm_2O_3 (8.9± 0.13), and Y_2O_3 (9.0) as shown in Fig. (**7b**). To prepare stable suspensions, the pH of solvent should be adjusted far from IEP, in order to provide zeta potential values above 20mV. On the other hand, to disperse at least two different powders (p_a and p_b), it is desired to set the pH of solvent near the IEP of one of the powders, *e.g.*, p_a. As a result, a layer of particles will be

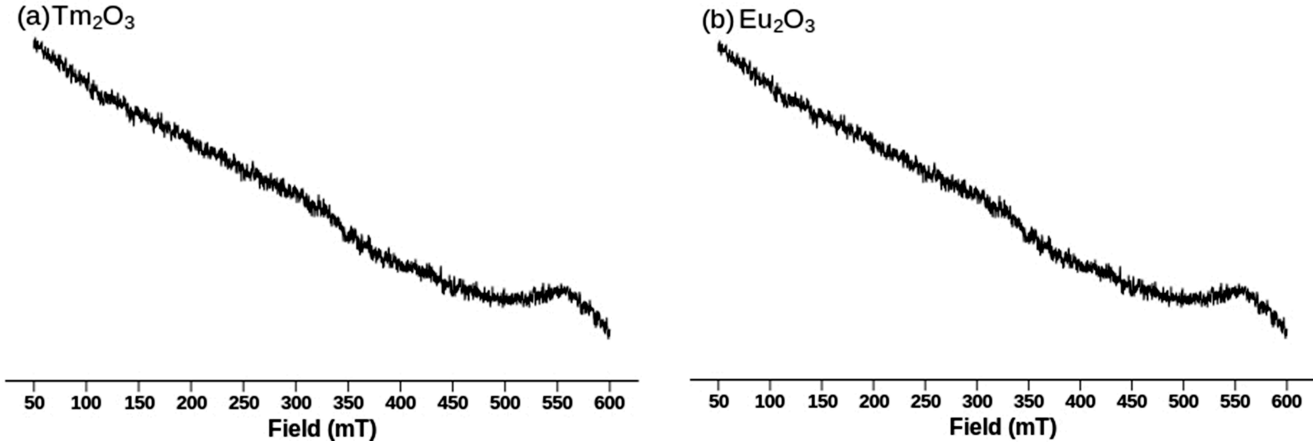

Fig. (6). EPR spectra of RE_2O_3 powders recorded under environmental temperature: (**a**) Tm_2O_3 and (**b**) Eu_2O_3. (*A higher resolution / colour version of this figure is available in the electronic copy of the article*).

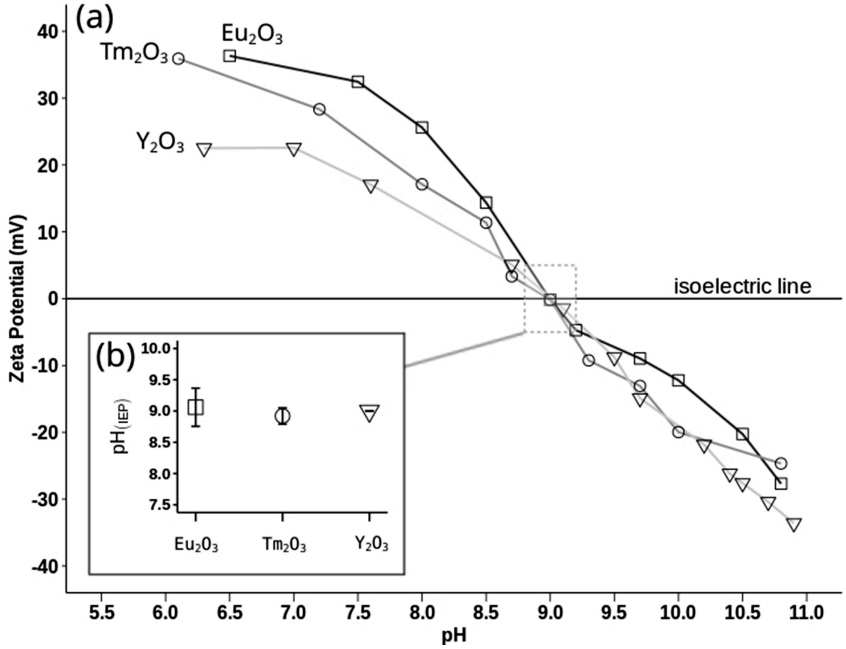

Fig. (7). Stability of RE_2O_3 particles in aqueous solvent: (**a**) zeta potential curves of colloidal suspensions based on Eu_2O_3, Tm_2O_3, and Y_2O_3 powders recorded under environmental temperature; (**b**) isoelectric point of the colloidal suspensions. (*A higher resolution / colour version of this figure is available in the electronic copy of the article*).

formed in the bottom (p_a), and finally, the separation from the other powder (p_b) occurs.

The results of zeta potential characterization of yttria were in agreement with those reported previously in our investigations [65, 66]. Yttria aqueous suspensions exhibited IEP at pH 8.5, and stability condition in pH range from pH 5.5 up to pH 7 (ζ of |50 mV|), and from pH 9.5 up to pH 12, in which ζ of 40 mV was recorded at pH 10.5.

A project of a new dosimetric material often demands a set of procedures, such as the selection of the starting materials, followed by synthesis methods, shaping, and sintering. The characterization of the starting materials provides substantial data to advance towards further processing stages and form advanced dosimetric materials based on rare-earth sesquioxides.

CONCLUSION

The characteristics of the three sesquioxides (RE_2O_3) powders, namely Tm, Eu, and Y, were evaluated as a bottom-up strategy to form functional materials for radiation dosimetry. All samples exhibited cubic C-type structure, a mean particle size distribution (d_{50}) inferior to 130 nm, flake-like morphology, and pycnometric density (ρ_p) values equivalent to 98 % theoretical density (ρ_t). As dispersed in an aqueous solvent, RE_2O_3 powders exhibited a mean isoelectric point at around pH 9 and were highly stable at pH 10.5. By Electron Paramagnetic Resonance, only Y_2O_3 powders presented resonance peaks, and the most significant signal was recorded at 358 mT and g 1.9701. The RE_2O_3 nanoparticles are promising materials to be used as activators of new materials for radiation dosimetry.

CURRENT FUTURE AND DEVELOPMENTS

Rare-earth sesquioxides comprehend as a selected group of base materials that have larger applicability, and their demand has been increased considerably. Powder characterization is a popular technique in ceramic processing and has a great implication with regard to rare-earth sesquioxides. Considering that the functionality of a ceramic component relies on starting materials (shape, size, density, chemical composition), referring to the powder characteristics, this theme will demand more investigations for further development.

ETHICS APPROVAL AND CONSENT TO PARTICIPATE

Not applicable.

HUMAN AND ANIMAL RIGHTS

No Animals/Humans were used for studies that are the basis of this research.

CONSENT FOR PUBLICATION

Not applicable.

AVAILABILITY OF DATA AND MATERIALS

Not applicable.

FUNDING

The authors would like to acknowledge the following sponsor organizations: São Paulo Research Foundation (FAPESP) (grant# 2018/05982-0), National Council for Scientific and Technological Development (CNPq) (grant# 426513/2018-5), and Coordination for the Improvement of High Degree People (CAPES).

CONFLICT OF INTEREST

The authors declare no conflict of interest, financial or otherwise.

ACKNOWLEDGEMENTS

The authors are deeply grateful to Dra. Maria Elisa Chuery Martins Rostelato from Radiation Technology Center (CTR) located at the Energy and Nuclear Research Institute (IPEN/CNEN-SP, Sao Paulo, Brazil) for allowing the use of particle size analyzer and MSc. They are also thankful to Beatriz Ribeiro Nogueira from the same centre for providing guidance in using the equipment.

REFERENCES

[1] Nanoparticle Technology Handbook. In: Nano Today, 2007; 2(4): pp. 45. https://doi.org/10.1016/S1748-0132(07)70119-6

[2] Thampi AD, Prasanth MA, Anandu AP, Sneha E, Sasidharan B, Rani S. The effect of nanoparticle additives on the tribological properties of various lubricating oils – Review. Mater Today Proc 2021; 47(15): 4919-24. https://doi.org/10.1016/j.matpr.2021.03.664

[3] Ortiz-Godoy N, Agredo-Diaz DG, Garzón-Posada AO, Parra Vargas CA, Landínez Téllez DA, Roa-Rojas J. A facile method to produce magnetic nanoparticles and its influence on their magnetic and physical properties. Mater Lett 2021; 293: 129700. http://dx.doi.org/10.1016/j.matlet.2021.129700

[4] Nofar M, Salehiyan R, Ray SS. Influence of nanoparticles and their selective localization on the structure and properties of polylactide-based blend nanocomposites. Compos, Part B Eng 2021; 215: 108845. http://dx.doi.org/10.1016/j.compositesb.2021.108845

[5] Fang C, Jing Z, Qin X, *et al.* Effect of heat treatment of green bodies on the sintering and optical properties of large-size and thick transparent YAG ceramics. Ceram Int 2021; 47: 9606-12. http://dx.doi.org/10.1016/j.ceramint.2020.12.097

[6] Abou-Elanwar AM, Shirke YM, Kwon SJ, *et al.* Size effects of carboxylated magnetite nanoparticles on the membrane dehumidification performance. J Environ Chem Eng 2021; 9: 105304. http://dx.doi.org/10.1016/j.jece.2021.105304

[7] Zahmatkesh I, Sheremet M, Yang L, *et al.* Effect of nanoparticle shape on the performance of thermal systems utilizing nanofluids: A critical review. J Mol Liq 2021; 321: 114430. http://dx.doi.org/10.1016/j.molliq.2020.114430

[8] Lavker RM, Kaplan N, McMahon KM, *et al.* Synthetic high-density lipoprotein nanoparticles: Good things in small packages. Ocul Surf 2021; 21: 19-26. https://doi.org/10.1016/j.jtos.2021.03.001

[9] Giraldo LJ, Diez R, Acevedo S, Cortés FB, Franco CA. The effects of chemical composition of fines and nanoparticles on inhibition of formation damage caused by fines migration: Insights through a simplex-centroid mixture design of experiments. J Petrol Sci Eng 2021; 203: 108494. http://dx.doi.org/10.1016/j.petrol.2021.108494

[10] Jain A, Wang YG, Guo H. Emergence of relaxor behavior along with enhancement in energy storage performance in light rare-earth doped Ba0.90Ca0.10Ti0.90Zr0.10O3 ceramics. Ceram Int 2021; 47: 10590-602. http://dx.doi.org/10.1016/j.ceramint.2020.12.171

[11] Bonfante MC, Raspini JP, Fernandes IB, Fernandes S, Campos LMS, Alarcon OE. Achieving sustainable development goals in

rare earth magnets production: A review on state of the art and SWOT analysis. Renew Sustain Energy Rev 2021; 137: 110616. http://dx.doi.org/10.1016/j.rser.2020.110616

[12] Ni S, Chen Q, Gao Y, Guo X, Sun X. Recovery of rare earths from industrial wastewater using extraction-precipitation strategy for resource and environmental concerns. Miner Eng 2020; 151: 106315. http://dx.doi.org/10.1016/j.mineng.2020.106315

[13] Weng W, Biesiekierski A, Lin J, Li Y, Wen C. Impact of rare earth elements on nanohardness and nanowear properties of beta-type Ti- 24Nb-38Zr-2Mo alloy for medical applications. Materialia (Oxf) 2020; 12: 100772. http://dx.doi.org/10.1016/j.mtla.2020.100772

[14] Deng S, Prodius D, Nlebedim IC, Huang A, Yih Y, Sutherland JW. A dynamic price model based on supply and demand with application to techno-economic assessments of rare earth element recovery technologies. Sustain Prod Consum 2021; 27: 1718-27. http://dx.doi.org/10.1016/j.spc.2021.04.013

[15] Costa L, Mirlean N, Johannesson KH. Rare earth elements as tracers of sediment contamination by fertilizer industries in Southern Brazil, Patos Lagoon Estuary. Appl Geochem 2021; 129: 104965. http://dx.doi.org/10.1016/j.apgeochem.2021.104965

[16] Jakoby M, Beil C, Nazari P, *et al.* Rare-earth coordination polymers with multimodal luminescence on the nano-, micro-, and milli-second time scales. iScience 2021; 24(3): 102207. http://dx.doi.org/10.1016/j.isci.2021.102207 PMID: 33733068

[17] Dushyantha N, Batapola N, Ilankoon IMSK, *et al.* The story of rare earth elements (REEs): Occurrences, global distribution, genesis, geology, mineralogy and global production. Ore Geol Rev 2020; 122: 103521. http://dx.doi.org/10.1016/j.oregeorev.2020.103521

[18] Department of the Interior. U.S.G.S.Mineral Commodity Summaries. A Federal Strategy to Ensure Secure and Reliable Supplies of Critical Minerals 2017. Available from: https://www.commerce.gov/news/reports/2019/06/federal-

[19] Fabrice M, Fulvio A, Silvia B, *et al.* Critical Raw Materials and the Circular Economy – Background report. 2017. http://dx.doi.org/10.2760/378123

[20] Jung HK, Kim CH, Hong A-R, *et al.* Luminescent and magnetic properties of cerium-doped yttrium aluminum garnet and yttrium iron garnet composites. Ceram Int 2019; 45: 9846-51. http://dx.doi.org/10.1016/j.ceramint.2019.02.023

[21] Magdalane CM, Kaviyarasu K, Vijaya JJ, *et al.* Evaluation on the heterostructured CeO_2/Y_2O_3 binary metal oxide nanocomposites for UV/Vis light induced photocatalytic degradation of Rhodamine - B dye for textile engineering application. J Alloys Compd 2017; 727: 1324-37. http://dx.doi.org/10.1016/j.jallcom.2017.08.209

[22] Ordoñez MFC, Amorim CLG, Krindges I, *et al.* Microstructure and micro-abrasive wear of sintered yttriacontaining 316L stainless steel treated by plasma nitriding. Surf Coatings Technol 2019; 374: 700-12. https://doi.org/10.1016/j.surfcoat.2019.06.002

[23] Raj AKV, Rao PP, Sreena TS, Thara TRA. .Pigmentary colors from yellow to red in $Bi_2Ce_2O_7$ by rare earth ion substitutions as possible high NIR reflecting pigments. Dye Pigment 2019; 160: 177-87. https://doi.org/10.1016/j.dyepig.2018.08.010

[24] Hastir A, Kohli N, Singh RC. Comparative study on gas sensing properties of rare earth (Tb, Dy and Er) doped ZnO sensor. J Phys Chem Solids 2017; 105: 23-34. http://dx.doi.org/10.1016/j.jpcs.2017.02.004

[25] Zhao F, Liang Y, Lee JB, Hwang SJ. Applications of rare earth Tb3+- Yb3+ co-doped down-conversion materials for solar cells. Mater Sci Eng B 2019; 248: 114404. http://dx.doi.org/10.1016/j.mseb.2019.114404

[26] Djamal M, Yuliantini L, Hidayat R, Boonin K, Yasaka P, Kaewkhao J. Glass medium doped rare earth for sensor material. Mater Today Proc 2018; 5: 15126-30. http://dx.doi.org/10.1016/j.matpr.2018.04.069

[27] Kershi RM. Rare-earth ions as a key influencer on the magnetic, spectroscopic and elastic properties of $ErγZn0.2Co0.8Fe_2−γO_4$ nanoparticles. J Alloys Compd 2021; 864: 158114. http://dx.doi.org/10.1016/j.jallcom.2020.158114

[28] Tscharnuter W. Photon Correlation Spectroscopy in Particle Sizing. 1st ed. United States of America: John Wiley & Sons Ltd 2000. http://dx.doi.org/10.1002/9780470027318.a1512

[29] Cullity BD. Elements of X-Ray Diffraction. Addition Wesley Publication Company, Addison Wesley Publication Company California 1956.

[30] Hanic F, Hartmanova M, Knab GG, Urusovskaya AA, Bagdasarov KS. Real Structure of Undoped Y_2O_3 Single-crystals. Acta Crystallogr B 1984; 40: 76-82. http://dx.doi.org/10.1107/S0108768184001774

[31] Cesaria M, Collins J, Di Bartolo B. On the efficient warm white-light emission from nano-sized Y_2O_3. J Lumin 2016; 169: 574-80. http://dx.doi.org/10.1016/j.jlumin.2015.08.017

[32] Zhang L, Jiang DY, Xia JF, Li CX, Zhang N, Li Q. Novel luminescent yttrium oxide nanosheets doped with Eu^{3+} and Tb^{3+}. RSC Advances 2014; 4: 17648-52. http://dx.doi.org/10.1039/c4ra01881h

[33] Yavetskiy RP, Baumer VN, Danylenko MI, *et al.* Transformation-assisted consolidation of $Y_2O_3:Eu^{3+}$ nanospheres as a concept to optical nanograined ceramics. Ceram Int 2014; 40: 3561-9. http://dx.doi.org/10.1016/j.ceramint.2013.09.072

[34] Han X, Feng X, Qi X, Wang X, Li M. The photoluminescent properties of $Y_2O_3:Bi^{3+}$, Eu^{3+}, Dy^{3+} phosphors for white-light-emitting diodes. J Nanosci Nanotechnol 2014; 14(5): 3387-90. http://dx.doi.org/10.1166/jnn.2014.8030 PMID: 24734556

[35] Alarcon-Flores G, Garcia-Hipolito M, Aguilar-Frutis M, *et al.* Luminescent and structural characteristics of Y2O3:TB3+ thin films as a function of substrate temperature. ECS J Solid State Sci Technol 2014; 3: R189-94. http://dx.doi.org/10.1149/2.0141410jss

[36] Qin X, Ju Y, Bernhard S, Yao N. Flame synthesis of Y_2O_3:Eu nanophosphors using ethanol as precursor solvents. J Mater Res 2005; 20: 2960-8. http://dx.doi.org/10.1557/JMR.2005.0364

[37] Gourlaouen V, Schnedecker G, Lejus AM, Boncoeur M, Collongues R. Metastable phases in yttrium oxide plasma spray deposits and their effect on coating properties. Mater Res Bull 1993; 28: 415-25. http://dx.doi.org/10.1016/0025-5408(93)90123-U

[38] Navrotsky A, Benoist L, Lefebvre H. Direct calorimetric measurement of enthalpies of phase transitions at 2000°–2400°C in Yttria and Zirconia. J Am Ceram Soc 2005; 88: 2942-4. doi:10.1111/j.1551-2916.2005.00506.x

[39] Santos SC, Yamagata C, Campos LL, Mello-Castanho SRH. Bioprototyping and thermoluminescence response of cellular rare earth ceramics. J Eur Ceram Soc 2016; 36: 791-6. http://dx.doi.org/10.1016/j.jeurceramsoc.2015.10.024

[40] Riener K, Albrecht N, Ziegelmeier S, *et al.* Influence of particle size distribution and morphology on the properties of the powder feedstock as well as of AlSi10Mg parts produced by laser powder bed fusion (LPBF). Addit Manuf 2020; 34: 101286. http://dx.doi.org/10.1016/j.addma.2020.101286

[41] Yi BJ, Zhang LQ, Mao ZH, Huang F, Zheng CG. Effect of the particle size on combustion characteristics of pulverized coal in an O_2/CO_2 atmosphere. Fuel Process Technol 2014; 128: 17-27. http://dx.doi.org/10.1016/j.fuproc.2014.06.025

[42] Telegin SV, Kirillova NI, Modin IA, Suleimanov EV. Effect of particle size distribution on functional properties of Ce0.9Y0.1O2-d ceramics. Ceram Int 2021; 47(12): 17316-21. https://doi.org/10.1016/j.ceramint.2021.03.043

[43] Liu D, Li Y, Lv C, *et al.* Permeating behaviour of porous SiC ceramics fabricated with different SiC particle sizes. Ceram Int 2021; 47: 5610-6. http://dx.doi.org/10.1016/j.ceramint.2020.10.145

[44] Minami T, Wang WN, Iskandar F, Okuyama K. Photoluminescence properties of submicrometer phosphors with different crystallite/particle sizes. Jpn J Appl Phys 2008; 47: 7220-3. http://dx.doi.org/10.1143/JJAP.47.7220

[45] Permin DA, Kurashkin SV, Novikova AV, *et al.* Synthesis and luminescence properties of Yb-doped Y_2O_3, Sc_2O_3 and Lu_2O_3 solid solutions nanopowders. Opt Mater 2018; 77: 240-5. https://doi.org/10.1016/j.optmat.2018.01.041

[46] Shivaramu NJ, Lakshminarasappa BN, Nagabhushana KR, Singh F. Synthesis characterization and luminescence studies of gamma irradiated nanocrystalline yttrium oxide. Spectrochim Acta A Mol Biomol Spectrosc 2016; 154: 220-31. http://dx.doi.org/10.1016/j.saa.2015.09.019 PMID: 26529639

[47] Carregosa JDC, Grilo JPF, Godoi GS, Macedo DA, Nascimento RM, Oliveira RMPB. Microwave-assisted hydrothermal synthesis

of ceria (CeO2): Microstructure, sinterability and electrical properties. Ceram Int 2020; 46: 23271-5.
http://dx.doi.org/10.1016/j.ceramint.2020.06.021

[48] Chan JX, Wong JF, Hassan A, Shrivastava NK, Mohamad Z, Othman N. Green hydrothermal synthesis of high aspect ratio wollastonite nanofibers: Effects of reaction medium, temperature and time. Ceram Int 2020; 46: 22624-34.
http://dx.doi.org/10.1016/j.ceramint.2020.06.025

[49] Tomina VV, Stolyarchuk NV, Katelnikovas A, *et al.* Preparation and luminescence properties of europium(III)-loaded aminosilica spherical particles. Colloids Surf A Physicochem Eng Asp 2021; 608: 125552.
http://dx.doi.org/10.1016/j.colsurfa.2020.125552

[50] Kawai Y, Yamamoto T. Synthesis of porous carbon hollow particles maintaining their structure using hyper-cross-linked Poly(St-DVB) hollow particles. Adv Powder Technol 2020; 31: 614-20.
http://dx.doi.org/10.1016/j.apt.2019.11.016

[51] Mema I, Wagner EC, van Ommen JR, Padding JT. Fluidization of spherical *versus* elongated particles - experimental investigation using X- ray tomography. Chem Eng J 2020; 397: 125203.
http://dx.doi.org/10.1016/j.cej.2020.125203

[52] Chang T-H, Lu Y-C, Yang M-J, Huang J-W, Chang L. Multi-branched flower-like ZnO particles from eco-friendly hydrothermal synthesis as green antimicrobials in agriculture. J Clean Prod 2020; 262: 121342.
http://dx.doi.org/10.1016/j.jclepro.2020.121342

[53] Nandi S, Sommerville L, Nellenbach K, *et al.* Platelet-like particles improve fibrin network properties in a hemophilic model of provisional matrix structural defects. J Colloid Interface Sci 2020; 577: 406-18.
http://dx.doi.org/10.1016/j.jcis.2020.05.088 PMID: 32502667

[54] Okada S, Takagi K, Ozaki K. Synthesis of submicron-sized acicular goethite and platelet-like hematite particles and dependence of magnetic properties of α-Fe particles on their shape and size. Mater Chem Phys 2016; 171: 171-7.
http://dx.doi.org/10.1016/j.matchemphys.2016.01.002

[55] Dupont A, Largeteau A, Parent C, Le Garrec B, Heintz JM. Influence of the yttria powder morphology on its densification ability. J Eur Ceram Soc 2005; 25: 2097-103.
http://dx.doi.org/10.1016/j.jeurceramsoc.2005.03.016

[56] Faithful DB, Johnson SM, Mccolm IJ. Infrared-spectra of lanthanide sesquioxides. Rev Chim Miner 1973; 10: 291-302.

[57] Lakshminarasappa BN, Shivaramu NJ, Nagabhushana KR, Singh F. Synthesis characterization and luminescence studies of 100 MeV Si^{8+} ion irradiated sol gel derived nanocrystalline Y_2O_3. *Nucl. Instruments Methods Phys. Res. Sect. B-Beam Interact. with Mater.* Atoms 2014; 329: 40-7.
http://dx.doi.org/10.1016/j.nimb.2014.02.128

[58] Hari Krishna R, Nagabhushana BM, Nagabhushana H, *et al.* Auto-ignition based synthesis of Y_2O_3 for photo- and thermo-luminescent applications. J Alloys Compd 2014; 585: 129-37.
http://dx.doi.org/10.1016/j.jallcom.2013.09.037

[59] Mangalaraja RV, Mouzon J, Hedström P, Camurri CP, Ananthakumar S, Odén M. Microwave assisted combustion synthesis of nanocrystalline yttria and its powder characteristics. Powder Technol 2009; 191: 309-14.
http://dx.doi.org/10.1016/j.powtec.2008.10.019

[60] Ahmed F, Kumar S, Arshi N, Anwar MS, Koo BH, Lee CG. Doping effects of Co^{2+} ions on structural and magnetic properties of ZnO nanoparticles. Microelectron Eng 2012; 89: 129-32.
http://dx.doi.org/10.1016/j.mee.2011.03.149

[61] Mu Q, Wang Y. A simple method to prepare $Ln(OH)_3$ (Ln = La, Sm, Tb, Eu, and Gd) nanorods using CTAB micelle solution and their room temperature photoluminescence properties. J Alloys Compd 2011; 509: 2060-5.
http://dx.doi.org/10.1016/j.jallcom.2010.10.141

[62] Cui F, Zhang J, Cui T, *et al.* A facile solution-phase approach to the synthesis of luminescent europium methacrylate nanowires and their thermal conversion into europium oxide nanotubes. Nanotechnology 2008; 19(6): 065607.
http://dx.doi.org/10.1088/0957-4484/19/6/065607 PMID: 21730705

[63] Wang S, Gu F, Li C, Lü M. Synthesis of Mesoporous Eu_2O_3 Microspindles. Cryst Growth Des 2007; 7: 2670-4.
http://dx.doi.org/10.1021/cg070111a

[64] Bordun OM, Dmitruk VV. Luminescence centers in thin films of yttrium oxide and yttrium-aluminum garnet activated with bismuth. J Appl Spectrosc 2008; 75: 208-13.
http://dx.doi.org/10.1007/s10812-008-9029-2

[65] Osipov VV, Rasuleva AV, Solomonov VI. Luminescence of pure yttria. Opt Spectrosc 2008; 105: 524-30.
http://dx.doi.org/10.1134/S0030400X08100068

[66] Santos SC, Acchar W, Yamagata C, Mello-Castanho S. Yttria nettings by colloidal processing. J Eur Ceram Soc 2014; 34: 2509-17.
http://dx.doi.org/10.1016/j.jeurceramsoc.2014.03.006